The Horizontal Momentum Balance in the Marine Atmospheric Boundary Layer during CODE-2*

R. M. SAMELSON AND S. J. LENTZ

Woods Hole Oceanographic Institution, Woods Hole, Massachusetts

(Manuscript received 24 January 1994, in final form 9 May 1994)

ABSTRACT

The horizontal momentum balance in the marine atmospheric boundary layer during the Coastal Ocean Dynamics Experiment (CODE) is analyzed, using meteorological data from an array of surface moorings. Previous studies have indicated the presence of orographically generated mesoscale features that are induced by strong southward flow around Point Arena. The present analysis demonstrates that during periods of strong southward flow, the cross-shore momentum equation is dominated by a balance between the ageostrophic acceleration associated with the flow curvature around Point Arena, and the cross-shore pressure gradient, while the alongshore momentum equation is dominated by a balance between vertical stress divergence and alongshore pressure gradient. These balances are consistent with results from a shallow water model of the marine layer. The calculations provide evidence for orographic modification of the horizontal structure of the boundary layer under a broader range of southward flow conditions than had been indicated by previous studies.

1. Introduction

Physical oceanographers interested in the coastal ocean have in recent years found it increasingly important to determine the mesoscale (10–100 km) structure of the coastal marine atmospheric boundary layer, in order to understand the ocean circulation driven by—or coupled to—the flux of momentum (wind stress) and other quantities across the air–sea interface. Thus, during the Coastal Ocean Dynamics Experiment (CODE), which took place off the west coast of the United States in spring and summer of 1981 and 1982, extensive moored and aircraft meteorological measurements were made in addition to the suite of oceanographic measurements.

A study of the CODE meteorological data that focused on the aircraft measurements led to the hypothesis that mesoscale variations in wind speed and wind stress could be generated by the interaction of hydraulically supercritical southward winds with the coastal orography (Dorman 1985; Winant et al. 1988). This hypothesis was supported by the results of a comparison of the data to a steady shallow-water model of flow in a hydraulically supercritical boundary layer (Samelson 1992).

These analyses suggested that the meteorological array deployed during CODE should have resolved the dominant orographically generated mesoscale structure of the wind field relatively well. In the present study, we use the CODE moored array dataset to investigate the horizontal momentum balance in the marine atmospheric boundary layer in detail. We compare the results of this analysis with momentum balances from the dynamical model developed by Samelson (1992) and to previous estimates from aircraft observations by Zemba and Friehe (1987).

The dataset is described briefly in section 2. The analysis of the observed momentum balances is presented in section 3 and compared with the model results in section 4. Section 5 contains a summary.

2. Observations

We have restricted the analysis to the observations obtained during the 1982 experiment, denoted CODE-2, because the data coverage for surface pressure is better for CODE-2 than for CODE-1 (1981). The data come from two sources: a set of surface buoys deployed specifically for CODE-2 by the Woods Hole Oceanographic Institution, and a pair of long-term monitoring buoys deployed and maintained by the National Oceanographic and Atmospheric Administration (NOAA). Both sets of moorings, the instruments deployed on each, and the data processing procedures, have been described in detail elsewhere (Limeburner 1985; Beardsley et al. 1987). An overview of meteorological conditions during CODE has been given by Beardsley et al. (1987).

Corresponding author address: Dr. Roger M. Samelson, Woods Hole Oceanographic Institution, Woods Hole, MA 02543.

Meteorological measurements were obtained at the WHOI buoys N3, C2, C3, C4, C5, and R3, and at the NOAA buoys NDBO13 and NDBO14, for a common period spanning 15 April–2 July 1982. The locations of these buoys are indicated in Fig. 1. Vector-averaged winds from a 3-cup anemometer and vane at 3.5-m altitude were recorded every 7.5 minutes at all the WHOI buoys. Barometric pressure was also recorded every 7.5 minutes at C3 and C5. Average wind speed and direction from a propellor and vane at 10-m altitude, and barometric pressure were recorded every 8.5 minutes at the NOAA buoys. The WHOI sensors have an estimated uncertainty of $< 5\%$ for wind speed, $3.1°$ for wind direction, and 0.3 mb for pressure. The NOAA sensors have an estimated uncertainty of 10% for wind speed, $10°$ for wind direction, and 1 mb for pressure.

For the present analysis, the resulting time series were averaged to hourly values. Wind stress was calculated from the vector-averaged one-hour wind time series using the bulk aerodynamic method of Large and Pond (1981) and assuming neutral stability. The 10-m wind velocities at NDBO13 and NDBO14 were adjusted to the 3.5-m height of the WHOI wind observations using

$$\mathbf{u}(3.5) = \mathbf{u}(10) + \frac{\mathbf{u}_*}{\kappa} \log(3.5/10),$$

where κ is von Kármán's constant. The resulting decrease in NDBO wind speeds was typically about 10%. Estimates of stress using bulk formulas with stability corrections provided by R. Beardsley, which are modifications of those suggested by Liu et al. (1979), differed from the neutral estimates by typically 5% or less, and required an assumed value for the relative humidity, so the neutral estimates were used in the present analysis. (The effect of the stability corrections on the wind speed adjustment for NDBO13 and NDBO14 was also negligible, less than 0.2 m s^{-1} except at a few times.) Barometric pressure was corrected from instrument height to sea level using a constant air density of 1.2 kg m^{-3}.

3. Results

We have separately analyzed "alongshore" and "cross-shore" horizontal momentum balances in the marine atmospheric boundary layer. The coordinate system adopted was that used for analysis of the oceanographic observations, in which the alongshore coordinate (y) is positive along 317°N (true), approximately parallel to the 90-m isobath at mooring C3 (Fig. 1). This is approximately parallel to contours of the coastal orography as well, so the coordinate system is also appropriate for the meteorological analysis. The cross-shore coordinate (x) is normal to the alongshore coordinate and positive onshore. We write the corresponding horizontal momentum equations as

$$u_t + uu_x + vu_y - fv + p_x/\rho_a + \tau^x/(\rho_a H) = 0 \quad (1a)$$

$$v_t + uv_x + vv_y + fu + p_y/\rho_a + \tau^y/(\rho_a H) = 0, \quad (1b)$$

where (u, v) are the (x, y) components of velocity, f is the Coriolis parameter (9×10^{-5} s^{-1}), p is the pressure, ρ_a is the air density (1.2 kg m^{-3}), (τ^x, τ^y) is the surface stress (flux of momentum from atmosphere to ocean), and subscripts denote partial differentiation with respect to x, y, or time t. Equations (1) are an approximation to the exact horizontal momentum equations at the fixed level of the wind and pressure measurements, in which the vertical stress divergence has been estimated as τ/H, and the vertical advection and horizontal diffusion of horizontal momentum have been neglected. The horizontal momentum equations for Samelson's (1992) shallow-water model of the CODE marine boundary layer, which assumes that momentum is vertically mixed over the depth H of the layer, have essentially the same form as (1), so the momentum balances in the observations and the model may be compared directly.

The marine boundary layer in the CODE region during the spring and summer is typically capped by a temperature inversion (Beardsley et al. 1987). The inversion height is typically less than the height of the coastal mountains, which thus form a barrier to onshore flow in the boundary layer. Measurements of the inversion height are available from aircraft flights at only a few locations on selected days during CODE-2 (Friehe 1984). For the analysis of the time series to be presented below, we have therefore chosen $H = 100$ m in (1). In fact, the available observations indicate that H (when it could be estimated) varied significantly in both time and space. The errors associated with this approximation and others are discussed below.

The wind time series at C3 and C5 are dominated by several periods of strong (5–15 m s^{-1}) southward winds that persist for 5–15 days and are interrupted by shorter periods of weak (0–5 m s^{-1}) winds (Fig. 2). During the strong southward winds, there is a consistent 3–5 m s^{-1} component directed offshore at the offshore mooring C5, and a weaker component with diurnal variations directed onshore at the onshore mooring C3. This veering is evident in the mean wind vectors from the periods of southward flow shown in Fig. 3. (For this calculation, the criterion for strong southward flow was that the alongshore flow at NDBO14 was southward and greater than 5 m s^{-1}.) The veering is evidently induced by the coastal orography, as the flow near the coast parallels the coastline southeast from Point Arena, while the flow farther offshore continues more directly southward.

Winant et al. (1988) identified three characteristic flow patterns observed during CODE aircraft flights. Two of these, denoted "Pattern 2" and "Pattern 3," had strong (at least 8 m s^{-1}) southward flow. Pattern 2 had relatively uniform wind speeds, while Pattern 3
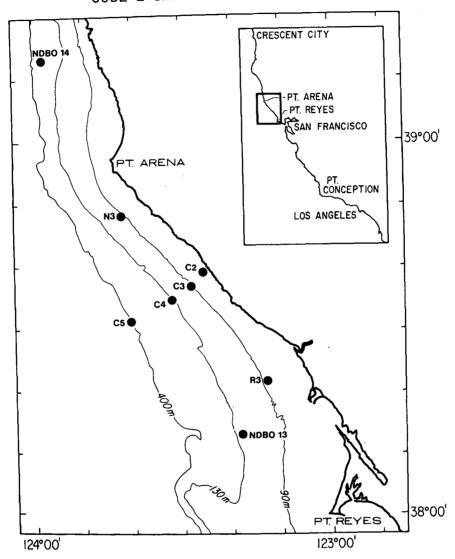
FIG. 1. Moorings with meteorological instrumentation during CODE-2. The cross-shore and alongshore coordinates are normal and parallel, respectively, to the 90-m isobath near C3.

had mesoscale variations in wind speed of 3–5 m s^{-1} or more (at 33 m altitude), as well as variations in wind direction. Dorman (1985), Winant et al. (1988), and Samelson (1992) have suggested that the interaction of the strong southward flow with the coastal orography causes the Pattern 3 mesoscale wind features. The momentum balances computed below demonstrate the importance of ageostrophic terms that are evidently associated with the flow curvature induced by the orography. However, the balances show no evidence for two separate dynamical regimes for southward flow, indicating that orographically induced flow curvature is also present in the Pattern 2 wind fields. Reexamination of the aircraft data (Friehe and Winant 1984,

1986) supports this interpretation, in that mesoscale variations in wind direction (with flow at the inshore moorings veering to follow the coastline more closely than flow at the offshore moorings) are evident in the Pattern 2 wind fields.

a. Cross-shore momentum balance

The terms in the cross-shore momentum equation (1a) were estimated as follows

$$u_t = [u_a(t + \Delta t) - u_a(t)]/\Delta t, \quad \Delta t = 1 \text{ h}$$

$$uu_x = u_a(u_{C3} - u_{C5})/\Delta x, \quad \Delta x = 19.7 \text{ km}$$
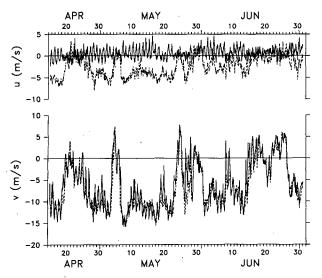
FIG. 2. Time series of cross-shore (u) and alongshore (v) wind speeds at C3 (solid) and C5 (dashed).

$$vu_y = 0.5(v_{N3} + v_{C3})(u_{N3} - u_{C3})/\Delta y_1,$$

$$\Delta y_1 = 30.0 \text{ km}$$

$$fv = fv_a$$

$$p_x = (p_{C3} - p_{C5})/\Delta x$$

$$\tau^x = 0.5(\tau^x_{C3} + \tau^x_{C5}),$$

where

$$u_a = 0.5(u_{C3} + u_{C5}), \quad v_a = 0.5(v_{C3} + v_{C5}).$$

Time series of these quantities for the entire CODE-2 period are shown in Fig. 4. The dominant balance is between the cross-shore pressure gradient p_x and the ageostrophic acceleration vu_y associated with the flow curvature induced by the bend in the coastline at Point Arena. The Coriolis term (which might be expected to balance p_x in the absence of alongshore variations in the coastal orography) is also significant, with uu_x and stress somewhat smaller. The local acceleration u_t is negligible.

A scatterplot of the two dominant terms is shown in Fig. 5. The correlation between them is 0.93. (For the 1862 hour time series with typical decorrelation time scale of 2 days, we estimate 38 degrees of freedom, for a 99.9% confidence level for nonzero correlation of 0.51.) Note that they are derived from completely independent observations: the pressure gradient from pressure measurements, and vu_y from wind measurements. For large (negative) cross-shore pressure gradients, there is a strong diurnal signal in pressure gradient and in vu_y. This is evidently a signature of the diurnal circulation previously observed during CODE (Beardsley et al. 1987). We do not pursue the investigation of these diurnal modulations here. The zero-lag correlation coefficients of p_x with the other terms are given in Table 1.

A scatterplot of the acceleration and stress terms (all the terms obtained from wind measurements) versus the pressure gradient is shown in Fig. 6. The regression line for acceleration and stress versus pressure has slope near 0.5 rather than 1. Given the strong correlation between p_x and vu_y indicated in Figure 5, it is likely that at least part of the error arises because the alongshore array resolution (N3, C3, R3) is not sufficient to resolve the alongshore gradient of cross-shore velocity, u_y. For example, if Δy_1 were reduced by half, but the alongshore difference in u were unchanged, the estimated terms in the momentum equation would nearly balance. Other possible explanations for the discrepancy seem less likely. Pressure transducer calibration errors of a factor of 2 in gain at both C3 and C5 can be ruled out, while a measurement or calibration error at just one of C3 or C5 would lower the high correlation with the independently measured vu_y term. The estimates of local acceleration u_t and Coriolis force $-fv$ do not require any spatial differencing, so an error in these would have to arise directly from the wind measurements. The stress divergence τ^x/H was obtained from bulk formulas rather than direct measurement, but it is not highly correlated with p_x and vu_y, and is unlikely to have been underestimated by the factor of 4 that would be required to balance the residual. Entrain-
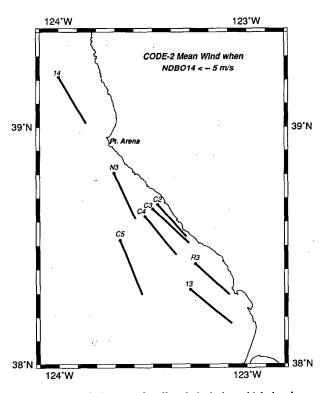

FIG. 3. Mean wind vectors for all periods during which the alongshore winds at NDBO14 were southward and greater than 5 m s^{-1}. The length of each vector is proportional to the mean wind speed at the corresponding mooring. The mean wind speed at NDBO13 is 10.0 m s^{-1}.
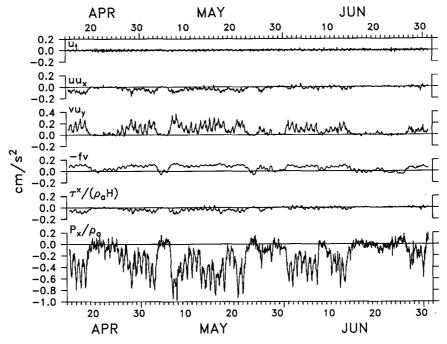
FIG. 4. Terms in the cross-shore momentum balance (1a) at C3 versus time for CODE-2.

ment stress could make up part of the difference, but available measurements (Zemba and Friehe 1987) suggest that it is small relative to the surface stress. Finally, the formulation (1) neglects the term wu_z, but this term should not be large near the sea surface where the measurements were made, since the mean vertical velocity w will be small. (The array resolution is addressed again below when the model momentum balances are discussed.)

Although pressure measurements were not available from N3 or R3, it is possible to estimate the spatial variation of the degree of ageostrophy of the flow by comparing the inertial acceleration terms (uu_x and vu_y) to the Coriolis force (fv) upstream and downstream of the C line. Time series of vu_y and $-fv$ estimated from the buoy pairs N3–C3, C5–NDBO13, and C3–R3 are
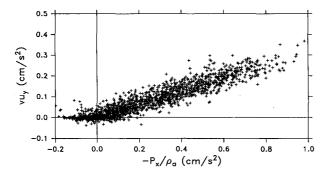

FIG. 5. Alongshore acceleration of cross-shore velocity vu_y versus cross-shore pressure gradient at C3.

shown in Fig. 7. Both the upstream (N3–C3) and offshore downstream (C5–NDBO13) estimates indicate a strongly ageostrophic flow, while the inshore downstream estimate (C3–R3) suggests a nearly geostrophic boundary layer flow. Similarly, time series of uu_x and $-fv$ estimated at the C line (C3–C5) and downstream (R3–NDBO13) are shown in Fig. 8. The C line estimate indicates strongly ageostrophic flow, while the downstream estimate suggests nearly geostrophic flow. (The local acceleration u_t and stress $\tau^x/\rho_a H$ are both small relative to fv at C3, R3, and NDBO13.)

The pressure gradient p_x and Coriolis force fv were previously computed from the same observations by Winant et al. (1988), who used the imbalance between them to argue for the presence of an ageostrophic component to the flow. Our results indicate that this ageostrophic component (vu_y) can be approximately calculated from the moored observations.

Zemba and Friehe (1987) estimated the pressure gradient p_x, Coriolis force fv, and stress divergence (the

TABLE 1. Zero-lag correlation coefficients between terms in the cross-shore (upper panel) and alongshore (lower panel) momentum balances. The estimated 99.9% confidence level for nonzero correlation is 0.51.

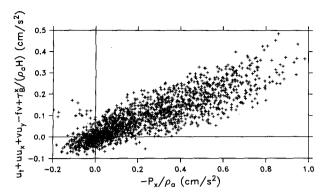|	u_t	uu_x	vu_y	$-fv$	τ^x/H
$-p_x$	−0.04	−0.50	0.93	0.83	−0.45
$-p_y$	0.05	0.33	0.44	−0.31	0.82

FIG. 6. Cross-shore acceleration and stress terms versus cross-shore pressure gradient at C3.

latter directly from flux measurements) along several transects of two CODE-1 aircraft flights. They also found an imbalance between the pressure gradient and the other terms, and inferred the presence of an ageostrophic balance. Their estimates of the vu_y term resulted in an approximate balance for one transect, but not for other transects.

To summarize, the dominant balance in the cross-shore momentum equation at the C line is between the ageostrophic acceleration associated with the flow curvature around Point Arena and the cross-shore pressure gradient. A transition to nearly geostrophic boundary layer flow apparently occurs downstream of the C line and inshore of NDBO13.

b. Alongshore momentum balance

The terms in the alongshore momentum equation (1b) were estimated at C3 and at C5, as follows.

At C3:

$$v_t = [v_{C3}(t + \Delta t) - v_{C3}(t)]/\Delta t$$

$$uv_x = u_{C3}(v_{C3} - v_{C5})/\Delta x$$

$$vv_y = v_{C3}(v_{N3} - v_{C3})/\Delta y_1$$

$$fu = fu_{C3}$$

$$p_y = (p_{NDBO14} - p_{C3})/\Delta y_2, \quad \Delta y_2 = 81.0 \text{ km}$$

$$\tau^y = \tau_{C3}^y.$$

At C5:

$$v_t = (v_{C5}(t + \Delta t) - v_{C5}(t))/\Delta t$$

$$uv_x = u_{C5}(v_{C3} - v_{C5})/\Delta x$$

$$vv_y = v_{C5}(v_{C5} - v_{NDBO13})/\Delta y_3, \quad \Delta y_3 = 44.8 \text{ km}$$

$$fu = fu_{C5}$$

$$p_y = (p_{C5} - p_{NDBO13})/\Delta y_3$$

$$\tau^y = \tau_{C5}^y \text{ or } \tau_{NDBO13}^y.$$

(Some of these terms could have been estimated in forms more precisely analogous to corresponding terms in the cross-shore momentum balance. The above forms were chosen in order to enhance the independence of the estimates at C3 and C5.)

The time series of the terms at C3 are shown in Fig. 9. The dominant balance is between the pressure gradient and the wind stress. The alongshore acceleration vv_y can be appreciable when the alongshore pressure gradient is large, but is dominated by diurnal variations. The local acceleration v_t is only significant at high frequencies, and the Coriolis term fu and the acceleration uv_x are essentially negligible. (The zero-lag correlation coefficients of p_y with the other terms are given in Table 1.) The pressure gradient and wind stress also dominate the balance at C5 and NDBO13.

Scatterplots of pressure gradient versus wind stress at C3 and NDBO13 are shown in Fig. 10. The slope of a best-fit line to these plots is near 1, particularly at C5 (not shown) and NDBO13. This may be partly fortuitous, since the choice of $H = 100$ m for the stress divergence is motivated only by a few observations and the model calculations below, and since the estimates of p_y may be too small (as for vu_y above). To estimate the alongshore pressure gradient p_y, the calculation at C3 uses the upstream (NDBO14) pressure, while the calculation at C5 uses the downstream (NDBO13) pressure. The estimate of the pressure gradient at C3 is almost certainly too small, since NDBO14 is 20 km north of Point Arena, and so does not resolve the adjustment of the flow to the coastline bend at Point Arena. The C5 pressure gradient may be too small for a similar reason. Note that the downstream (C5) balance is computed offshore, in the downstream region
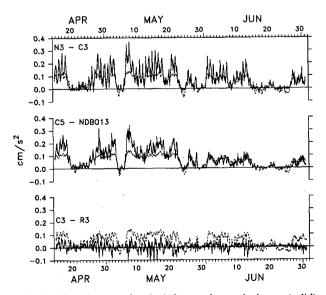

FIG. 7. Alongshore acceleration of cross-shore velocity vu_y (solid) and Coriolis acceleration $-fv$ (dashed) from N3–C3, C5–NDBO13, and C3–R3 versus time for CODE-2.
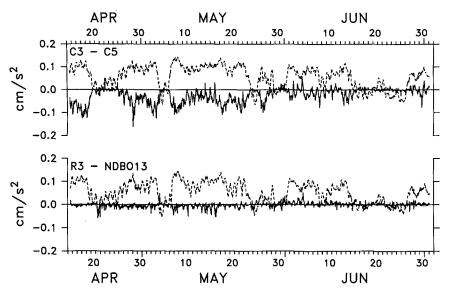
FIG. 8. Cross-shore acceleration of cross-shore velocity uu_x (solid) and Coriolis acceleration $-fv$ (dashed) from C3–C5 and R3–NDBO13 versus time for CODE-2.

that showed a cross-shore momentum balance similar to that upstream, rather than the geostrophic cross-shore balance that appears to hold inshore downstream. In both scatterplots, the distributions do not intercept the origin. This may be due to a bias error in the alongshore pressure gradient estimates, since a direct comparison of pressure calibrations between the NDBO and CODE buoys was not possible.

Zemba and Friehe (1987) estimated the pressure gradient p_y, Coriolis force fu, and stress divergence (the latter directly from flux measurements) along several transects of two CODE-1 aircraft flights. They also found an approximate balance between the pressure gradient and stress divergence.

To summarize, the dominant balance in the alongshore momentum equation near the C line is between
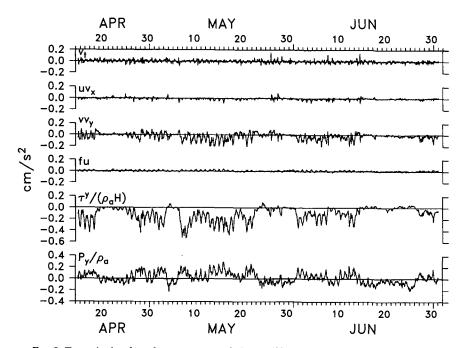

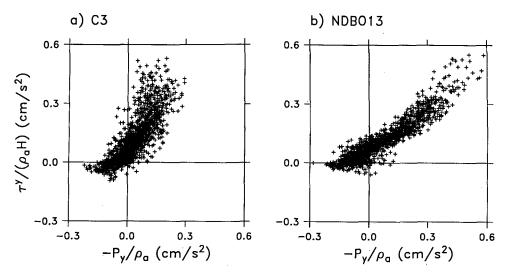FIG. 9. Terms in the alongshore momentum balance (1b) at C3 versus time for CODE-2.

FIG. 10. Alongshore stress τ^y/H versus alongshore pressure gradient p_y at (a) C3 and (b) NDBO13.

the alongshore pressure gradient and the vertical divergence of the alongshore wind stress. The alongshore acceleration of alongshore velocity is also significant, particularly near the diurnal frequency.

4. Model comparison

Samelson (1992) has developed a steady shallow water model of the marine atmospheric boundary layer for the hydraulically supercritical case. The model equations are similar to (1), with an additional (continuity) equation for the layer thickness, and with time derivatives neglected. The details of the model fields depend on parameters that in general are not well known from the observations: the upper level (i.e., just above the inversion capping the boundary layer) pressure gradient, the strength of the inversion, and the upstream normal-to-shore profiles of wind speed and marine-layer height. However, for a reasonable range of physically relevant parameter values, the qualitative features of the model fields are relatively constant, and these features may be compared to the observations.

a. Mesoscale pressure gradients

The model marine-layer thickness field is consistently characterized by a severe downstream shallowing along the coast. The thickness of the boundary layer increases rapidly offshore, reaching values comparable to the upstream thickness along a line that extends offshore and downstream from the Point Arena bend at an angle that depends on the upstream thickness and wind speed. An example is shown in Fig. 11a. (For purposes of comparison, approximate positions in the model flow corresponding to the geographical locations of the observational moorings are also shown. The parameters for the computation are given in section 4b.) The thick-

ness typically decreases along the coast to 20%–30% of its upstream value near the offshore bend south of Point Arena. The imposed upper-level pressure gradient must generally be oriented in a northwestward direction in order to maintain the supercritical flow conditions in the model, and while its magnitude can be appreciable, it does not dramatically alter the surface pressure field that results from the mesoscale deformations in the marine layer thickness. As a result, there is a characteristic ratio of the differences between the upstream (NDBO14) pressure, and the inshore (C3) and offshore (C5) pressure along the "C line" in the model. This ratio $(p_{NDBO14} - p_{C3}):(p_{NDBO14} - p_{C5})$ is typically 2:1. A scatterplot of these two quantities from the observations (Fig. 12) indicates that $p_{NDBO14} - p_{C3}$ tends to be larger than $p_{NDBO14} - p_{C5}$ for the northward pressure gradients (positive Δp) associated with southward winds. This feature appears to be robust in both the model and the observations, and in both, the associated large offshore pressure gradient between C3 and C5 is balanced by nonlinear accelerations (see below and section 3a). (Note that the distribution in Fig. 12 does not intercept the origin. This may indicate a bias in the differences of NDBO and CODE buoy pressures; see section 3b.) The large observed C3–C5 pressure gradients are almost certainly due primarily to variations in the marine-layer thickness, since persistent 0.5–2 mb differences in upper-level pressure over 20 km are highly unlikely.

b. Horizontal momentum balances

The structure of the model wind fields depends more strongly on the parameters than does the structure of the model-layer thickness. In general, the model wind fields have three dominant features: a region of acceleration south of the Point Arena bend, a region of de-
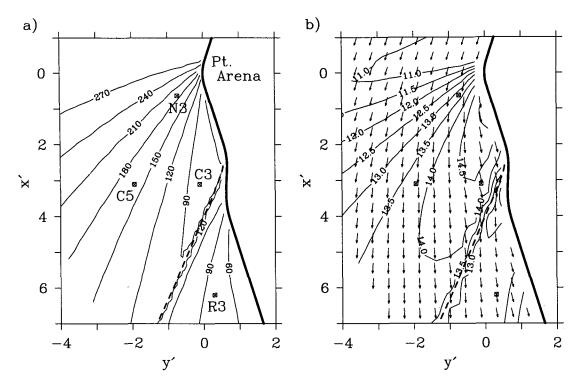
FIG. 11. Model fields: (a) marine-layer thickness (m) and (b) wind velocity and speed (m s^{-1}). The locations of the hydraulic jump (dashed line) and the observational moorings ($\boxtimes$) are indicated. The unit of horizontal distance is 10 km.

celeration south of the acceleration region, and a hydraulic jump (compression shock) induced by the offshore coastline bend south of Point Arena (Fig. 11). The position and intensity of these features all change significantly with parameters. For the case shown in Fig. 11, the imposed upper-level pressure gradient (in the model coordinate system) was $(P_{x'}, P_{y'}) = (-0.54, -0.88)$ mb/100 km, and the upstream marine-layer thickness was 300 m at the coast. This may be compared with the wind field shown in Fig. 7a of Samelson (1992), for which the upstream layer thickness was 210 m at the coast and the imposed pressure gradient was stronger and aligned more alongshore, $(P_{x'}, P_{y'}) = (-1.25, -0.65)$ mb/100 km, but all other parameters were the same. In the present case, the wind accelerates from 10 m s^{-1} upstream to 14 m s^{-1} near the C line, and then decelerates to 12 m s^{-1} at the southern edge of the computational domain. In contrast, the field shown in Fig. 9a of Samelson (1992) accelerates from 16 m s^{-1} to only 17.5 m s^{-1}, and then decelerates to 12 m s^{-1}. In that case, the deceleration begins 15–25 km farther north than in the present case, a distance comparable to the separation of the C3 and N3 moorings. The corresponding thickness fields (Fig. 11a above and Samelson's Fig. 7b) do not differ as dramatically.

The terms in the momentum balances for the model field shown in Fig. 11 are contoured in Figs. 13 and 14. From section 3, the observed local accelerations are

negligible for both cross-shore and alongshore balances, consistent with the steady model. The remaining terms may be compared directly.

Upstream of the bend, where the flow is parallel to the coast, the normal-to-shore (not the same upstream as the cross-shore direction introduced above and used below, which is normal-to-shore in the region just south of the Point Arena bend) balance is geostrophic, and
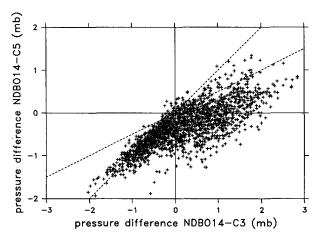

FIG. 12. Pressure difference NDBO14–C5 versus pressure difference NDBO14–C3. The dashed lines have slope 0.5 and 1.
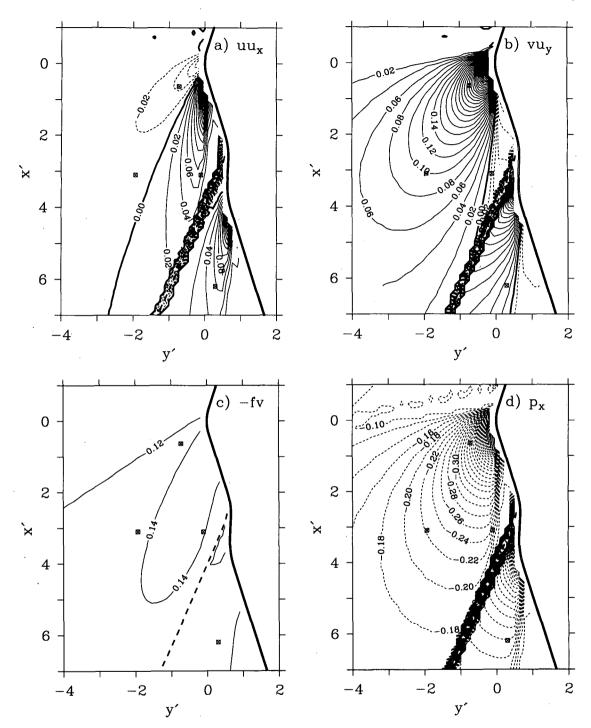
FIG. 13. Terms in the cross-shore momentum balance for the model fields shown in Fig. 9:
(a) uu_x, (b) vu_y, (c) $-fv$, (d) p_x, (e) τ^x/h. Contour interval: 0.02 cm s^{-2}.

the parallel-to-shore balance is between the imposed pressure gradient (since the marine-layer thickness is uniform parallel-to-shore upstream of the bend) and the stress. In the cross-shore and alongshore system in which the momentum balance is analyzed, geostrophy still dominates the upstream cross-shore balance, and stress and pressure gradient the upstream alongshore balance.

In general, the balances near C3 and C5 in the model agree with the observed balances. The cross-shore bal-
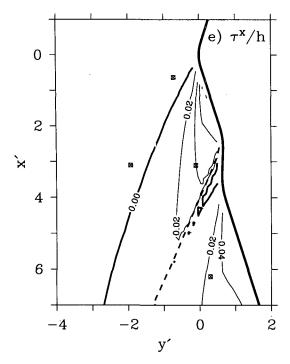
FIG. 13. (Continued)

ance is dominated by the ageostrophic term vu_y, the pressure gradient p_x, and the Coriolis term fv (Fig. 13). The term vu_y, while not large at C3 itself in the model, was calculated in the observations using an alongshore difference between C3 and N3, where the term is large in the model. This suggests that vu_y is resolved only in a spatially averaged manner by the observations. Near R3, the ageostrophic terms appear to be relatively small compared to the Coriolis acceleration (which is balanced primarily by the pressure gradient in the model), consistent with the observed estimates. Note, however, that there are large values of vu_y between C3 and R3 in the model, while the observational estimate from the alongshore difference between C3 and R3 is small.

Pressure gradient and stress dominate the model alongshore balance near C3 and C5, with the acceleration vv_y also appreciable (Fig. 14). The same terms dominate the observed balances. The structure of the model vv_y field, with a zero crossing between C3 and N3, suggests that an average value for it computed from N3 and C3 will be particularly sensitive to small variations in the flow conditions. This may be part of the cause of the high frequency (diurnal) signal in the estimate of vv_y in Fig. 9.

5. Summary

We have computed estimates of the acceleration, pressure gradient, Coriolis, and stress divergence terms in the horizontal momentum equations for the marine atmospheric boundary layer near the center of the

moored array deployed during CODE-2. During strong southward flow, the cross-shore balance is dominated by pressure gradient p_x, alongshore acceleration of cross-shore velocity vu_y, and Coriolis force fv. The alongshore balance is dominated by pressure gradient p_y and stress τ^y, with alongshore acceleration of alongshore velocity vv_y significant particularly near the diurnal frequency. The high correlations between independently estimated terms suggest that although the array does not fully resolve the spatial scales of the mesoscale features associated with strong southward flow around Point Arena, it does resolve the dominant dynamical balances that characterize the features. These results are consistent with previous calculations by Zemba and Friehe (1987) and Winant et al. (1988).

The mesoscale variability is more consistently evident in boundary layer thickness and wind direction than wind speed. There is evidence from the momentum balance analysis for orographic modification of the horizontal structure of the boundary layer thickness and wind direction for the Pattern 2 winds identified by Winant et al. (1988), as well as for Pattern 3, which was characterized by mesoscale structure in the wind speed, but there is no indication of the presence of two separate dynamical regimes for southward flow. Instead, the analysis suggests that both patterns arise within a single dynamical flow regime. An examination of the sensitivity of the model of Samelson (1992) to various parameters suggests that the upstream marine layer thickness may determine whether Pattern 2 or Pattern 3 winds prevail. When the upstream thickness is small, the effect of the downstream decrease in thickness on the vertical stress divergence (estimated here as $\tau/\rho_a H$) is relatively large, and mesoscale variations in wind speed (a downstream deceleration) arise. When the upstream thickness is large, the effect on the stress divergence is relatively small, and the wind speed is more uniform. The observations of Winant et al. (1988) appear to be consistent with this hypothesis, as Pattern 2 winds were generally associated with greater inversion heights (see their Table 1; note that Flight 2.24 should probably have been classified as Pattern 1 because of weak winds).

Following the suggestion of Dorman (1985) and Winant et al. (1988), the model of Samelson (1992) presumes that the flow in the marine layer can be treated as hydraulically supercritical, that is, that the speed U of the flow is faster than the maximum phase speed $c = (g'H)^{1/2}$ of gravity waves propagating horizontally on the inversion that caps the layer (or, equivalently, that the Froude number $Fr = U/c$ is greater than 1). It was not necessary to make any such assumption in analyzing the observed momentum balances. Because of the lack of vertical profile information, it was impossible to estimate the Froude number for the time series. Thus this analysis has not succeeded in directly determining whether and when the flow is supercritical. The agreement between observations and
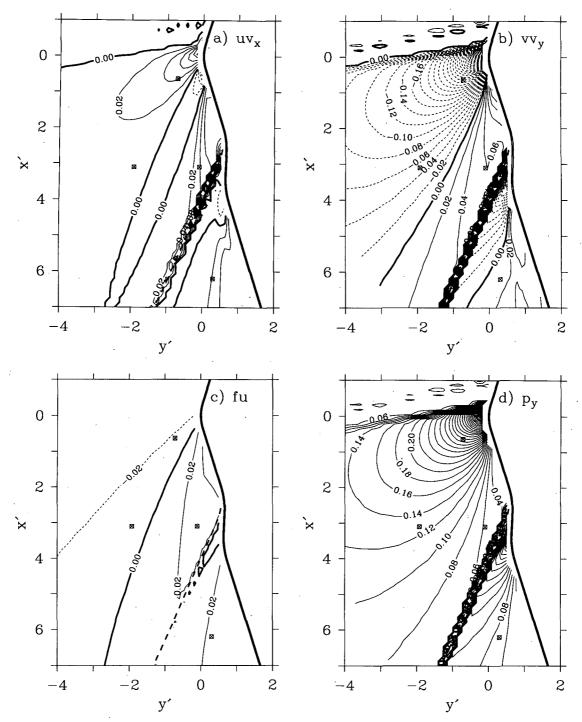
FIG. 14. Terms in the alongshore momentum balance for the model fields shown in Fig. 9: (a) uv_x, (b) vv_y, (c) fu, (d) p_y, (e) τ^y/h. Contour interval: 0.02 cm s^{-2}.

the supercritical model found here and by Samelson (1992) is indirect evidence that the strong southward flows (both Pattern 2 and Pattern 3) are supercritical, as is the consistent presence of large quasi-steady ageostrophic mesoscale pressure gradients (Fig. 12), which

presumably would be more likely to relax toward geostrophy under subcritical conditions, in which the propagation of gravity waves is not restricted.

Insofar as the supercriticality assumption was made to obtain insight into the flow dynamics, the present

where the nondimensionalized time is just

$$\tau = u_0 k t. \tag{13}$$

The corresponding harmonic expansions of the continuity equation (5) give

$$i \frac{\partial h_1}{\partial \tau} + u_1 + u_2 h_{-1} + u_{-1} h_2 = 0 + O(\epsilon^4) \tag{A5}$$

and

$$\frac{i}{2} \frac{\partial h_2}{\partial \tau} + u_2 + u_1 h_1 = 0 + O(\epsilon^4). \tag{A6}$$

With one self-iteration, (A5) provides the velocity field expression

$$u_1 = -i \frac{\partial h_1}{\partial \tau} - u_2 h_{-1} - i h_2 \frac{\partial h_{-1}}{\partial \tau} + O(\epsilon^4), \tag{A7}$$

which can then be used in (A6) to produce

$$u_2 = -\frac{i}{2} \frac{\partial h_2}{\partial \tau} + i h_1 \frac{\partial h_1}{\partial \tau} + O(\epsilon^3). \tag{A8}$$

The forms (A7), (A8) are now used to eliminate the velocity fields from (A3) and (A4). After much tedious but straightforward algebra this provides the expressions of the main text

$$\frac{d^2 h_1}{d\tau^2} + s^2 h_1 = \frac{C_D}{h_0 k} \left(\frac{i}{2} - \frac{d}{d\tau} \right) h_1 + P[|h_1|^2 h_1]$$

$$+ \frac{iC_D}{2h_0 k} Q[|h_1|^2 h_1] + R[h_2 h_1^*] + \frac{iC_D}{2h_0 k} S[h_2 h_1^*] \tag{12}$$

and

$$\frac{d^2 h_2}{d(2\tau)^2} + \frac{C_D}{h_0 k} \frac{dh_2}{d2\tau} + \left(s^2 - \frac{iC_D}{2h_0 k} \right) h_2$$

$$= \frac{1}{2} \frac{\partial}{\partial \tau} \left(h_1 \frac{\partial h_1}{\partial \tau} \right) + \frac{1}{2} \left(1 + \frac{iC_D}{2kh_0} \right) \left(\frac{\partial h_1}{\partial \tau} \right)^2$$

$$- \frac{iC_D}{4kh_0} h_1^2 + O(h_1^3). \tag{54}$$

REFERENCES

Brown, R. A., 1980: Longitudinal instabilities and secondary flow in the planetary boundary layer: A review. *Rev. Geophys. Space Phys.,* **18,** 683–697.

Chimonas, G., 1993: Surface drag instabilities in the atmospheric boundary layer. *J. Atmos. Sci.,* **50,** 1914–1924.

——, and C. J. Nappo, 1987: A thunderstorm bow wave. *J. Atmos. Sci.,* **44,** 533–541.

Doviak, R. J., and R. Ge, 1984: An atmospheric solitary gust observed with a Doppler radar, a tall tower and a surface network. *J. Atmos. Sci.,* **41,** 2559–2573.

Etling, D., and S. Raasch, 1987: Numerical simulation of vortex roll development during a cold air outbreak. *Dyn. Atmos. Oceans,* **10,** 277–290.

Jeffreys, H., 1925: The flow of water in an inclined channel of rectangular section. *Phil. Mag.,* **49,** 793–807.

Landau, L. D., and E. M. Lifshitz, 1959: *Fluid Mechanics.* chap. 3. Pergammon Press, 536 pp.

Lemone, M., 1973: The structure and dynamics of horizontal roll vortices in the PBL. *J. Atmos. Sci.,* **30,** 1077–1091.

Lilley, D. K., 1966: On the instability of Ekman boundary layer flow. *J. Atmos. Sci.,* **23,** 481–494.

Mason, P. J., and R. I. Sykes, 1982: A two-dimensional numerical study of horizontal roll vortices in an inversion capped planetary boundary layer. *Quart. J. Roy. Meteor. Soc.,* **108,** 801–823.

Miles, J. W., 1961: On the stability of heterogeneous shear flows. *J. Fluid Mech.,* **10,** 496–508.

Smith, R. B., 1976: The generation of lee waves by the Blue Ridge. *J. Atmos. Sci.,* **33,** 507–519.

Smith, R. K., 1988: Travelling waves and bores in the lower atmosphere: The "Morning Glory" and related phenomena. *Earth-Sci. Rev.,* **25,** 269–290.

Sutton, O. G., 1977: *Micrometeorology.* Robert E. Krieger Publishing (Reprint of 1955 original), 333 pp.